Summertime upper tropospheric nitrous oxide over the Mediterranean as a footprint of Asian emissions

Yannick Kangah, Philippe Ricaud, Jean-Luc Attié, Naoko Saitoh, Didier Hauglustaine, Rong Wang, Laaziz El Amraoui, Régina Zbinden, Claire Delon

AGU PUBLICATIONS

JGR

Journal of Geophysical Research: Atmospheres

RESEARCH ARTICLE
10.1002/2016JD026119

Key Points:
- Consistency between GOSAT N_2O measurements and LMDz-OR-INCA model N_2O results
- Evidence of a link between summertime Asian N_2O Emissions and the Mediterranean tropospheric N_2O

Correspondence to:
Y. Kangah,
yannick.kangah@meteo.fr

Citation:
Kangah, Y., P. Ricaud, J.-L. Attié, N. Saitoh, D. A. Hauglustaine, R. Wang, L. El Amraoui, R. Zbinden, and C. Delon (2017), Summertime upper tropospheric nitrous oxide over the Mediterranean as a footprint of Asian emissions, *J. Geophys. Res. Atmos.*, *122*, 4746–4759, doi:10.1002/2016JD026119.

Received 28 OCT 2016
Accepted 28 MAR 2017
Accepted article online 29 MAR 2017
Published online 29 APR 2017

Summertime upper tropospheric nitrous oxide over the Mediterranean as a footprint of Asian emissions

Yannick Kangah[1], Philippe Ricaud[1], Jean-Luc Attié[1,2], Naoko Saitoh[3], Didier A. Hauglustaine[4], Rong Wang[4,5], Laaziz El Amraoui[1], Régina Zbinden[1], and Claire Delon[2]

[1]CNRM-GAME, Toulouse, France, [2]Laboratoire d'Aérologie, Université de Toulouse, Toulouse, France, [3]Center for Environmental Remote Sensing, Chiba University, Chiba, Japan, [4]Laboratoire des Sciences du Climat et de l'Environnement, Paris, France, [5]Department of Global Ecology, Carnegie Institution for Science, Stanford, California, USA

Abstract The aim of this paper is to study the transport of nitrous oxide (N_2O) from the Asian surface to the eastern Mediterranean Basin (MB). We used measurements from the spectrometer Thermal and Near infrared Sensor for carbon Observation Fourier transform spectrometer on board the Greenhouse gases Observing SATellite (GOSAT) over the period of 2010–2013. We also used the outputs from the chemical transport model LMDz-OR-INCA over the same period. By comparing GOSAT upper tropospheric retrievals to aircraft measurements from the High-performance Instrumented Airborne Platform for Environmental Research Pole-to-Pole Observations, we calculated a GOSAT High-performance Instrumented Airborne Platform for Environmental Research standard deviation (SD error) of ~2.0 ppbv for a single pixel and a mean bias of approximately −1.3 ppbv (approximately −0.4%). This SD error is reduced to ~0.1 ppbv when we average the pixels regionally and monthly over the MB. The use of nitrogen fertilizer coupled with high soil humidity during the summer Asian monsoon produces high N_2O emissions, which are transported from Asian surfaces to the eastern MB. This summertime enrichment over the eastern MB produces a maximum in the difference between the eastern and the western MB upper tropospheric N_2O (east-west difference) in July in both the measurements and the model. N_2O over the eastern MB can therefore be considered as a footprint of Asian summertime emissions. However, the peak-to-peak amplitude of the east-west difference observed by GOSAT (~1.4 ± 0.3 ppbv) is larger than that calculated by LMDz-OR-INCA (~0.8 ppbv). This is due to an underestimation of N_2O emissions in the model and to a relatively coarse spatial resolution of the model that tends to underestimate the N_2O accumulation into the Asian monsoon anticyclone.

1. Introduction

Nitrous oxide (N_2O) is produced in oceans and soils by microbial processes of nitrification and denitrification [*Butterbach-Bahl et al.*, 2013]. With a 120 year lifetime, N_2O is the third anthropogenic greenhouse gas after carbon dioxide (CO_2) and methane (CH_4) in terms of radiative forcing [*Ciais et al.*, 2014]. The N_2O radiative forcing contribution accounts for 6–15% of the greenhouse gas emission contribution to global warming. In spite of its far lower concentration in the atmosphere than CO_2, N_2O is a much more efficient greenhouse gas with a global warming potential of 265 over a 100 year time span. Although its main sink is photolysis in the stratosphere, an additional loss of N_2O comes from its reaction with excited atomic oxygen $O(^1D)$ in the stratosphere. This reaction is the main source of stratospheric nitrogen oxides [*Minschwaner et al.*, 1993] that are involved in stratospheric ozone destruction. It is therefore the main emitted ozone-depleting substance of the 21st century [*Ravishankara et al.*, 2009]. Moreover, N_2O volume mixing ratio (vmr) has increased at an average rate of 0.75 ppbv yr^{-1} since the late 1970s and is expected to increase until 2100 according to the Intergovernmental Panel on Climate Change climatic scenarios due to the increasing use of nitrogen fertilizers in agricultural activities [*Ciais et al.*, 2014]. In Asia, the use of nitrogen fertilizers in agriculture is increasing to meet the growing demand for food production, making China and India the first and second largest consumers and producers of nitrogen fertilizers (https://www.tfi.org/statistics/statistics-faqs), respectively.

At a global scale, the strongest N_2O sources are natural soil emissions with an emission rate of 6–7 TgN yr^{-1}, followed by emissions from agricultural sources (4.3–5.8 TgN yr^{-1}) [*Syakila and Kroeze*, 2011]. Soil moisture is the major driver of N_2O emissions whose maxima occur around 55% soil water content (SWC) [*Oswald et al.*, 2013].

The second main control variable for N_2O emissions by soils is the nitrogen content of the soil, which increases when fertilizers are added in agro systems [*Butterbach-Bahl and Dannenmann*, 2011].

Contrary to surface N_2O measurements from the World Meteorological Organization Global Atmosphere Watch Programme [*Tsutsumi et al.*, 2009], tropospheric N_2O measurements at global or regional scale have neither been widely performed nor widely used up to now like those of CH_4 or CO_2. Remote Fourier transform infrared measurements of total column N_2O are regularly performed within the Network for the Detection of Atmospheric Composition Change [*Zander et al.*, 2005]. There are also sporadic aircraft campaigns including the High-performance Instrumented Airborne Platform for Environmental Research Pole-to-Pole Observations (HIPPO) [*Kort et al.*, 2011] used in this paper. However, satellite observations of tropospheric N_2O profiles and N_2O total columns have been performed by using respectively the Atmospheric Infrared Sounder (AIRS) on board the AQUA platform and the Infrared Atmospheric Sounder Interferometer (IASI) on board the METOP A/B platforms. Consistent interannual trends of N_2O with surface measurements can be derived from AIRS measurements [*Xiong et al.*, 2014], and the African equatorial maximum during March–May can be observed by using IASI total column measurements [*Ricaud et al.*, 2009]. In addition, N_2O is retrieved simultaneously with methane from the thermal infrared measurements of the Greenhouse gases Observing SATellite (GOSAT) at a global scale. Since this study is the first use of GOSAT N_2O data, this data set is introduced in this paper.

In the context of monitoring pollution effects on regional climate, the Chemistry and Aerosol Mediterranean Experiment (ChArMEx) project aims, among other objectives, to understand the spatial and temporal evolutions of chemical compounds over the Mediterranean Basin (MB). In this framework and despite the fact that well-mixed greenhouse gases were not expected to have significant regional variations in the troposphere, a summertime peak in the difference between the eastern and the western MB of middle-to-upper tropospheric CH_4 has been attributed to the transport of pollutants from Asia via the Asian monsoon anticyclone to the eastern MB [*Ricaud et al.*, 2014]. Therefore, variations of long-lived species over the MB can probably be used as footprints of Asian emissions of pollutants. Following this previous work, the aim of this paper is to demonstrate the impact of the Asian N_2O emissions on the upper tropospheric N_2O over the eastern MB. First, we present the N_2O data from the GOSAT Thermal and Near infrared Sensor for carbon Observation Fourier transform spectrometer (TANSO-FTS) together with our validation of GOSAT upper tropospheric N_2O by using the HIPPO aircraft measurements and introduce the chemical transport model LMDz-OR-INCA. Second, we study the N_2O seasonal variability in the eastern and the western MBs as well as the east-west difference of N_2O seasonal variability. Then, we analyze the link between these variabilities and the Asian N_2O emissions via the summer Asian monsoon and its associated anticyclone. Before concluding, we discuss first the correlation between high precipitation rates associated with the monsoon period and high N_2O emissions over Asia. Then, we discuss the influence of horizontal resolution in the model and emission modeling as well as the vertical resolution of measurements on the assessed east-west difference of the MB upper tropospheric N_2O seasonal variability in the model and in the observations, respectively.

2. Data Sets

2.1. GOSAT/TANSO-FTS Data

The Japanese Ministry of the Environment, the Japanese National Institute for Environmental Studies, and the Japan Aerospace eXploration Agency developed the Sun-synchronous orbital satellite GOSAT platform [*Hamazaki et al.*, 2005] dedicated to the study of two greenhouse gases: CO_2 and CH_4. The platform was launched on 23 January 2009 carrying two sensors: a Fourier transform spectrometer (TANSO-FTS) and a Cloud and Aerosol Imager (TANSO-CAI) [*Yokota et al.*, 2009]. The TANSO-FTS is a nadir-viewing instrument using four spectral bands covering the thermal infrared (TIR) and the shortwave infrared domains (0.76, 1.6, 2.0, and 5.5–14.3 μm) [*Kuze et al.*, 2009] with a 10.5 km diameter of instrumental field of view and a spectral resolution of ~0.2 cm^{-1}. Along with CH_4 retrievals in the TIR, N_2O is also processed as a by-product by using a nonlinear optimal estimation retrieval method [*Saitoh et al.*, 2009] from the latest V1 retrieval algorithm [*Saitoh et al.*, 2016]. The retrieval has been performed in clear-sky conditions [*Eguchi and Yokota*, 2008] in which clouds are filtered by using cloud flags provided by the TANSO-CAI during daytime [*Ishida and Nakajima*, 2009; *Ishida et al.*, 2011] and on the basis of the TANSO-FTS TIR spectrum during nighttime [*Saitoh et al.*, 2016]. The N_2O-retrieved profiles have been obtained by

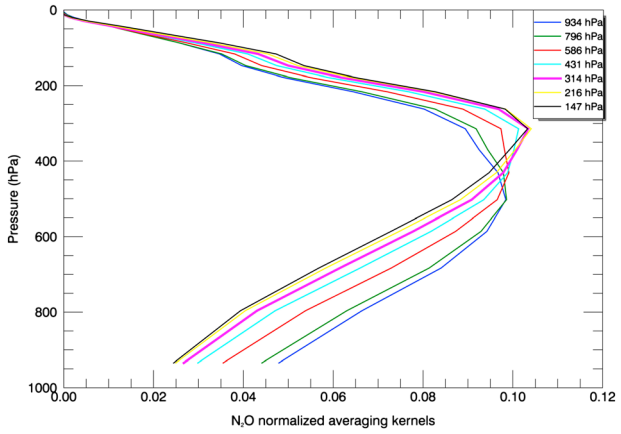

Figure 1. Normalized N_2O averaging kernels from GOSAT/TANSO-FTS at 35°N and 20°E and monthly averaged over July 2010. The different colors represent different retrieval representative levels as shown in the caption.

assuming a fixed a priori profile derived from the Michelson Interferometer for Passive Atmospheric Sounding (MIPAS) reference atmosphere (V3) climatology from 15°N to 60°N latitude (MIPAS reference atmosphere profiles can be downloaded from http://www.atm.ox.ac.uk/RFM/atm/).

GOSAT N_2O retrievals are performed on 22 retrieval grid layers, and each grid layer has a representative pressure level. The normalized averaging kernels shown in Figure 1 have been calculated at 35°N and 20°E and averaged over July 2010. They are representative of the MB since the N_2O averaging kernels do not have significant spatial variations over the MB. They characterize the sensitivity of GOSAT N_2O measurements at each of the 22 retrieval layers to the true atmospheric N_2O profile [*Rodgers*, 2000] (only seven of them are represented in Figure 1). The GOSAT N_2O-retrieved profiles reach a maximum of sensitivity between 500 and 200 hPa peaking at the pressure level of 314 hPa. Since we are studying upper tropospheric N_2O transport processes, 314 hPa will be the reference pressure level for our analyses.

Individual retrievals have total theoretical random errors less than 2% (~6.4 ppbv for 320 ppbv) at each retrieval level. In this study, we took averages (spatially and temporally) (monthly/interannually) of GOSAT N_2O data (see section 3.1) over the MB at 314 hPa instead of using the individual retrievals. The random errors on the N_2O averaged values are less than 0.1% (~0.3 ppbv). TIR measurements are highly affected by surface parameters such as surface emissivity and temperature [*Claeyman et al.*, 2011]. The errors in the surface parameters can impact the N_2O retrieval as systematic errors. Because surface parameters have generally high variability (e.g., diurnal amplitude of surface temperature), these errors may vary in time and space. Thus, to minimize the impact of systematic errors caused by surface parameters, we only used maritime pixels where these parameters exhibit much smaller variations than over land. In addition, consistent with the methodology presented in *Ricaud et al.* [2014] to minimize any systematic errors, we mostly analyze seasonal variability of differences such as anomalies and east-west differences over the MB (see section 3.1), assuming that systematic errors are of the same order of magnitude in the eastern and the western MBs.

Since we are interested in the N_2O variability, we determined the anomaly from its respective mean of all N_2O data over the latitude band 15°N–60°N for each year over the period of 2010–2013. This approach has the main advantage of facilitating the comparison between model results and measurements.

2.2. GOSAT N_2O Data Validation

In addition to the theoretical errors analysis presented in section 2.1, we used the HIPPO airborne campaigns to assess the quality of the GOSAT N_2O retrievals. The HIPPO campaigns performed in situ measurements over the Pacific Ocean by using the National Science Foundation's Gulfstream V aircraft. Several aerosols and chemical species including N_2O were measured over a wide range of latitudes (67°S–87°N) and altitudes (600–15,000 m) with vertical profiles every 2.2° of latitude [*Wofsy*, 2011, *Wofsy et al.*, 2012]. HIPPO encompasses five campaigns: HIPPO 1 (January 2009), HIPPO 2 (October–November 2009), HIPPO 3 (March–April 2010), HIPPO 4 (June–July 2011), and HIPPO 5 (August–September 2011). Since our GOSAT data cover the period of 2010–2013, we used the HIPPO campaigns 3–5 to assess the quality of the GOSAT N_2O retrievals (Figure 2). For our comparison, we used the measurements from the Harvard/Aerodyne Quantum Cascade Laser Spectrometer, one of the airborne instruments of HIPPO. This instrument has a 1σ precision of 0.09 ppbv and an accuracy of 0.2 ppbv [*Kort et al.*, 2011].

Each vertical profile from HIPPO is identified by its mean coordinates (latitude, longitude, and time) and is interpolated on the 22 retrieval representative levels of GOSAT. Since HIPPO profiles do not cover the

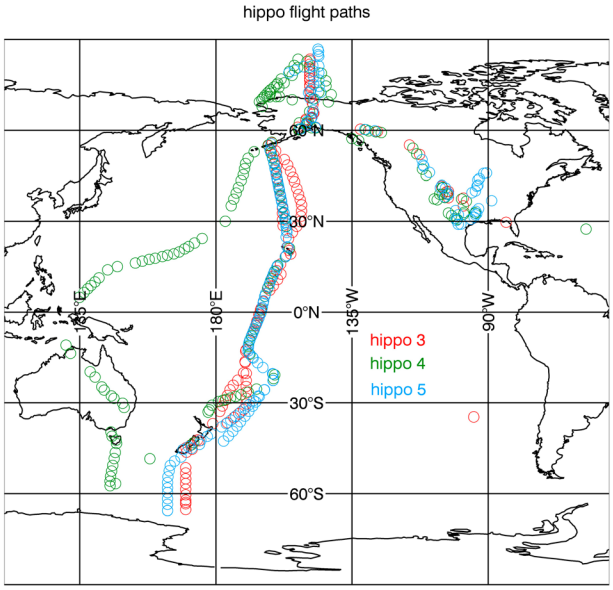

Figure 2. Flight paths of HIPPO campaigns used for GOSAT N_2O validation: HIPPO 3 (March–April 2010, red), HIPPO 4 (June–July 2011, green), and HIPPO 5 (August–September 2011, blue).

entire vertical range of GOSAT retrievals, we extended the HIPPO profiles to the bottom and to the top of the atmosphere by using monthly averaged profiles from LMDz-OR-INCA. However, to minimize the impact of such artificial extension on our validation results and since we are interested in the 314 hPa level, we only took HIPPO profiles with a ceiling pressure of less than 250 hPa and a bottom pressure level of greater than 400 hPa.

To evaluate only the retrieval system and not the instrumental performance of the TANSO-FTS sounder, we applied the GOSAT N_2O averaging kernel to the HIPPO measurements by using the following equation [*Rodgers*, 2000]:

$$\hat{x} = Ax + (I - A)x_a \quad (1)$$

where A is the averaging kernel matrix, I the identity matrix, x_a the a priori profile (the same used for GOSAT retrievals), x the HIPPO profile, and $\hat{x}$ the HIPPO convolved profile. Each HIPPO convolved profile is then compared to the GOSAT measurements in time and space coincidence considering GOSAT maritime profiles within a distance of ±300 km of the HIPPO profile and a temporal window of ±12 h. The standard deviation of the HIPPO N_2O data selected from all of the three campaigns at 314 hPa is ~3.3 ppbv. The standard deviation of the convolved HIPPO N_2O data at 314 hPa is ~2.0 ppbv. Therefore, the vertical sensibility of the GOSAT instrument represented by the averaging kernels tends to underestimate the variability of N_2O at 314 hPa.

Figure 3 shows the comparison between the GOSAT N_2O data retrievals and the HIPPO N_2O at 314 hPa by using 200 coincident pairs with our selection criteria. P_0 = 318.4 ppbv is the intersection point between the regression line and the first bisector (the line $y = x$). The Pearson linear correlation coefficient is about 0.44. The slope of the regression line is about ~0.22 ppbv ppbv^{-1}, which means that the GOSAT N_2O variations are smaller than HIPPO N_2O variations at 314 hPa. GOSAT data underestimate N_2O for volume mixing ratio (vmr) larger than P_0 and conversely for vmr smaller than P_0. This confirms the fact that, in general, the GOSAT retrieval system tends to reduce the amplitude of N_2O variations. Since N_2O is retrieved simultaneously with CH_4 in the GOSAT retrieval system, a strong constraint has been applied on N_2O in order to avoid large oscillations that could impact the CH_4 retrieval product. This strong constraint artificially reduces the GOSAT N_2O variability at 314 hPa.

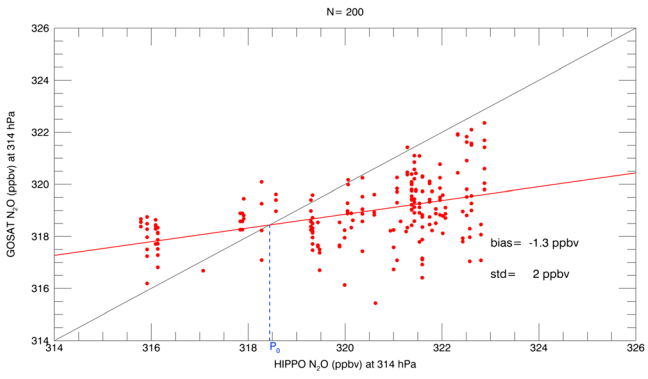

Figure 3. HIPPO (3–5) N_2O airborne measurements versus GOSAT N_2O at 314 hPa in time and space coincidence within a box of ±300 km and ±12 h. N (=200) is the total number of coincident pairs selected. The black and red lines represent the first bisector ($y = x$) and the linear regression line, respectively. The dashed blue line represents the intersection point (P_0 = 318.4 ppbv) of the regression line and the first bisector. Note that we applied the GOSAT averaging kernels on HIPPO observations.

The mean N_2O bias (GOSAT-HIPPO) at 314 hPa is about −1.3 ppbv (~0.4%) because tropospheric N_2O vmr are mostly greater than P_0. Furthermore, since HIPPO measurements have a very good precision (~0.03% at 320 ppbv), the standard deviation of the

GOSAT-HIPPO differences (called hereafter SD error), which is about 2.0 ppbv (~0.6%), can be considered as an estimation of the real random error on an individual GOSAT measurement. This value is small and much less than the theoretical value of 6.4 ppbv (~2%) (see section 2.1) associated with the total random error on a single retrieval.

To conclude, the comparisons with HIPPO data show that the GOSAT N_2O maritime pixels at 314 hPa are of sufficient quality to be used in order to analyze regional and seasonal N_2O variabilities. However, we have to keep in mind that the GOSAT retrieval system tends to underestimate the amplitude of the upper tropospheric N_2O variations. Furthermore, averaging spatially and temporally (between 400 and 900 profiles) over the eastern and the western MBs results in a very small random errors: less than ~0.3 ppbv (~0.09%) for the theoretical error and ~0.1 ppbv for the SD error. Thus, we also have to keep in mind that the error values used in our analysis of N_2O seasonal variabilities are calculated by using the theoretical total random errors which are much more pessimistic than the SD error from the comparison with HIPPO measurements.

2.3. LMDz-OR-INCA

The INteraction between Chemistry and Aerosol (INCA) model coupled with the general circulation model LMDz GCM is used to simulate the distribution of aerosols and gaseous reactive species in the troposphere [*Hauglustaine et al.*, 2004]. In addition, soil/atmosphere exchanges of water and energy are simulated by coupling LMDz with the Organizing Carbon and Hydrology in Dynamic Ecosystems dynamic global vegetation model [*Krinner et al.*, 2005]. Together, these three models form the LMDz-OR-INCA model. The model has a horizontal resolution of 1.26° in latitude and 2.5° in longitude and 39 vertical levels from the surface up to 80 km. The N_2O surface emissions are monthly averages based on *Thompson et al.* [2014] for anthropogenic and natural emissions and on the Global Fire Emissions Database version 4.1 (GFEDv4.1) inventory for biomass burning [*Giglio et al.*, 2013]. The total annual emission rate is 16.08 TgN yr^{-1} in our simulations. Our model is forced dynamically by the meteorological analysis from the European Centre for Medium-Range Weather Forecasts. We used monthly averaged N_2O outputs covering the period of 2010–2013 together with GOSAT retrievals to assess the impact of Asian summertime emissions on eastern MB upper tropospheric N_2O.

However, in order to assess the impact of improving the horizontal resolution and the surface emission inventories on the modeled N_2O transport, we used in section 4 another configuration of LMDz-OR-INCA referred to as LMDz-OR-INCA low resolution (LMDz-OR-INCA *low res*). LMDz-OR-INCA *low res* has been performed for climate change impact investigations by using different Representative Concentration Pathway scenarios [*Hauglustaine et al.*, 2014]. The horizontal resolution in this configuration is 1.9° in latitude and 3.75° in longitude. This configuration used monthly averaged N_2O surface emissions based on *Bouwman and Taylor* [1996] for anthropogenic and natural emissions and on the Global Fire Emissions Database version 3 inventory for biomass burning [*Van der Werf et al.*, 2010]. The total annual emission rate in this configuration is 13.27 TgN yr^{-1}. The vertical levels are the same in the two configurations.

3. Results

3.1. N_2O Variability Over the Mediterranean Basin

GOSAT and LMDz-OR-INCA anomalies have been calculated for each year from their annual mean over the latitude band 15°N–60°N. These anomalies are averaged monthly from 2010 to 2013 and selected within two boxes (36–45°N, 1–12°E) and (30–37°N, 26–37°E) to represent the western and eastern MBs (black boxes in Figure 4), respectively. Figure 4 shows the N_2O anomaly fields in summer (June, July, and August) and winter (December, January, and February) at 314 hPa observed by GOSAT and calculated by LMDz-OR-INCA. In winter, a very weak positive east-west N_2O difference is measured by GOSAT (~0.7 ppbv) and calculated by the model (~0.15 ppbv) with a larger anomaly over the eastern MB.

In summer, this gradient is enhanced within the two data sets, although it remains less intense in the model (~0.5 ppbv) compared to GOSAT (~1.5 ppbv). Figure 5 shows the seasonal variation of the N_2O anomaly observed by GOSAT and calculated by LMDz-OR-INCA for the two basins. In the GOSAT data, a seasonal cycle is observed in the eastern MB with a maximum in July and a peak-to-peak amplitude of ~1.8 ± 0.4 ppbv, whereas in the western MB, a maximum with a peak-to-peak amplitude of ~0.8 ± 0.4 ppbv is observed in August. The GOSAT peak in July over the eastern MB is sharper than the peak in August over the western

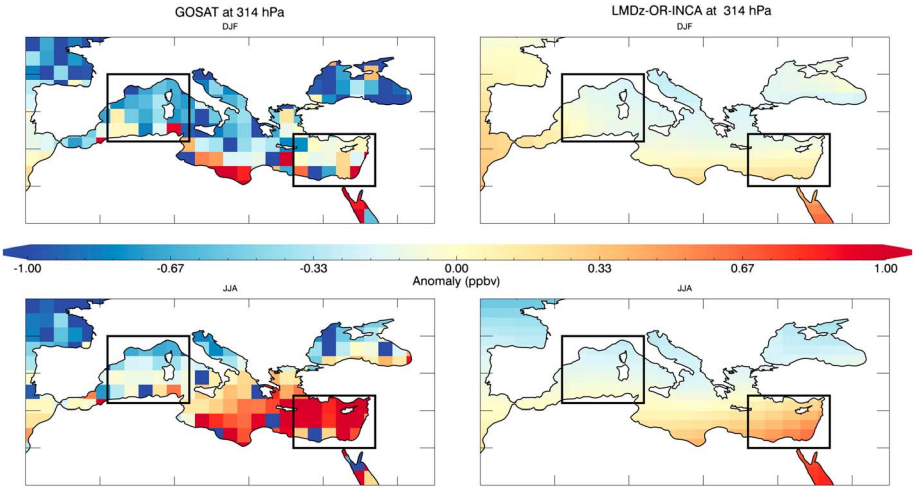

Figure 4. N_2O volume mixing ratio anomaly (ppbv) from (left) GOSAT TANSO-FTS (right) and LMDz-OR-INCA at 314 hPa for (top) December-January-February (DJF) and for (bottom) June-July-August (JJA) averaged over the period of 2010–2013. The satellite measurements and the model outputs are selected within the black boxes to represent the eastern and the western Mediterranean Basins.

MB. The error bars represent the random total errors on monthly averaged N_2O retrievals and indicate the confidence level on the mean value. Despite the small values of the seasonal amplitude, the seasonal cycle is statistically significant regarding measurements errors. Consistently with GOSAT anomalies, a seasonal cycle is also detected in LMDz-OR-INCA data but with a maximum from August to November in the eastern MB and from September to December in the western MB (peak-to-peak amplitude of ~1.5 ppbv in the two basins).

Figure 6 shows the N_2O difference between the eastern and the western MBs at 314 hPa called hereafter east-west difference. In GOSAT data, the monthly averaged east-west difference has no significant variations (~0.4 ± 0.8 ppbv) from January to May and starts to increase in June reaching a peak-to-peak amplitude of ~1.4 ± 0.3 ppbv in July before decreasing until November. The east-west difference in LMDz-OR-INCA follows almost the same seasonal variation but with a peak-to-peak amplitude less intense than in GOSAT (~0.8 ppbv). Although the two data sets are consistent with each other in terms of the seasonal variation of the east-west difference, the amplitude of the seasonal variations and the absolute value of the difference show inconsistencies. These differences are discussed in section 4. We note that the maximum of the east-west difference occurs in July in both the model results and in the GOSAT observations. The processes that govern this summertime N_2O increase over the eastern MB are investigated in the next section.

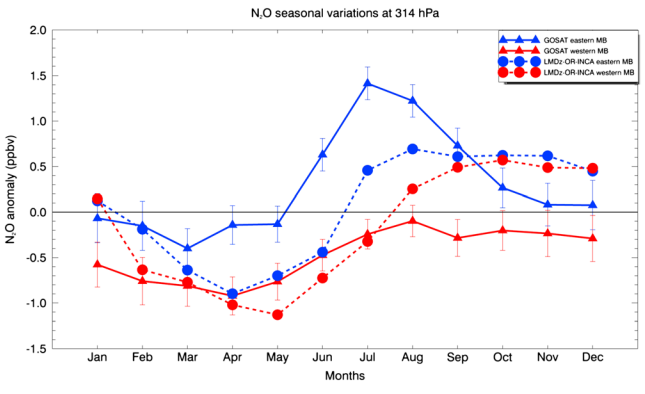

Figure 5. Seasonal variation of the monthly averaged N_2O anomalies (ppbv) from GOSAT TANSO-FTS (solid lines and triangles) and LMDz-OR-INCA (dashed lines and circles) at 314 hPa on the eastern (blue) and western (red) Mediterranean Basins averaged over the period of 2010–2013. The error bars represent the error on the mean considering the theoretical random error of the retrieval and the number of monthly averaged pixels.

3.2. Impact of Asian Summer Monsoon

Due to its particular location, the MB is influenced by several meteorological patterns and air masses originating from Europe, North Africa, the Arabian peninsula, North America, and Asia [*Ricaud et al.*, 2014]. Figure 7 shows the LMDz-OR-INCA northern hemisphere N_2O anomaly and wind patterns representative of the months of July and August (bottom) and the other months (top) over the period of 2010–2013 at 314 hPa.

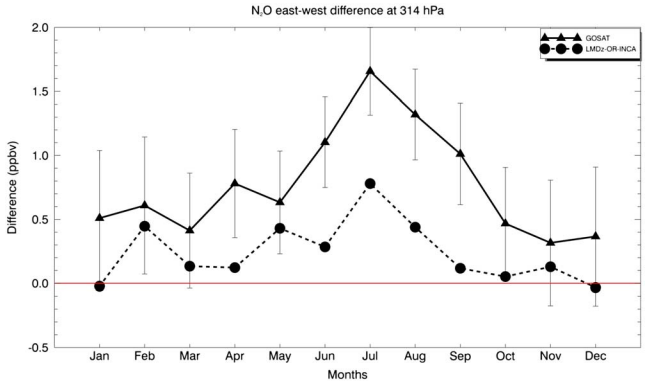

Figure 6. Seasonal variation of the east-west difference of N_2O (ppbv) measured by GOSAT TANSO-FTS (solid line) and calculated by LMDz-OR-INCA (dashed line) at 314 hPa. The error bars represent the error on the mean considering the theoretical random error of the retrieval and the number of monthly averaged pixels.

Upper tropospheric air masses over the eastern and western MBs mainly come from North America and the northern Atlantic throughout the year. But in summer, over the eastern MB, upper tropospheric air masses are mostly transported from Asia through the Asian monsoon anticyclone [*Scheeren et al.*, 2003; *Rodwell and Hoskins*, 1996] and are also influenced by the Arabian Peninsula and North Africa [*Dayan*, 1986; *Tyrlis et al.*, 2013].

The impact of long-range transport of air masses from Asia on the MB explains the maximum in the east-west CH_4 difference in the upper troposphere observed in August [*Ricaud et al.*, 2014]. Westerly circulation brings air masses from the northern Atlantic and North America from January until May. At the beginning of the Asian monsoon period in June, a southerly circulation takes place over the eastern MB, bringing tropical air masses from Asia to the eastern MB. These air masses are enriched in pollutants trapped by the monsoon anticyclone. Thus, pollutants emitted in Asia are transported to the upper troposphere by updrafts associated with the monsoon region and redistributed westward to the eastern MB by the monsoon anticyclone. In the next section, we investigate the different regions of N_2O emissions in Asia.

3.3. Asian N_2O Surface Emissions

The eastern MB air masses come from the Asian anticyclone in summer and are therefore impacted by the N_2O surface emissions from different Asian regions. Figure 8 synthesizes the pressure levels of air masses from 10 day back trajectories covering the period of 2001–2011 (two trajectories per day at 00:00 and 12:00 UTC) in July and in August from the point located at 33°N, 35°E and 300 hPa in the eastern MB. This back trajectory climatology has been performed by using the British Atmospheric Data Centre trajectory service

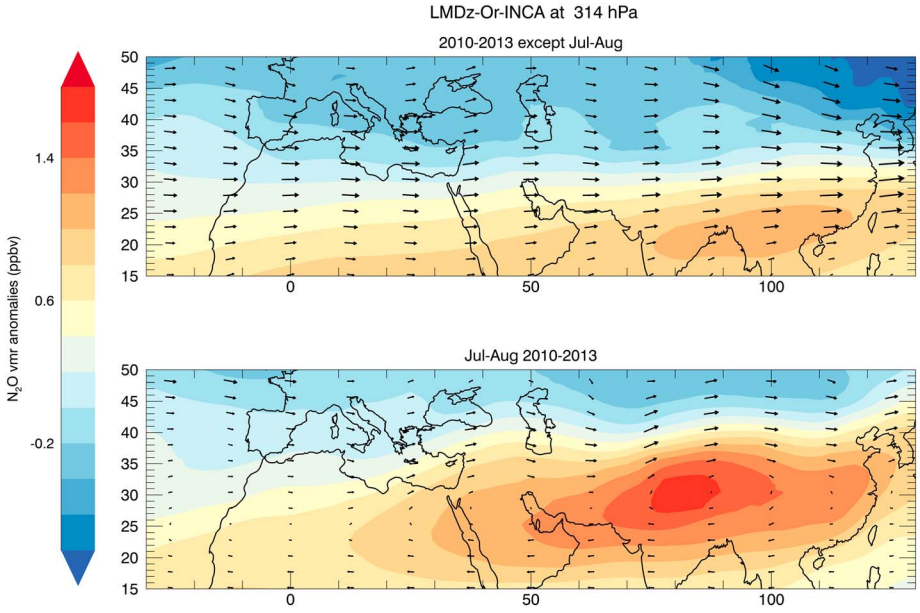

Figure 7. N_2O volume mixing ratio anomaly (ppbv) from LMDz-OR-INCA and horizontal wind from IFS at 314 hPa averaged over (bottom) July and August 2010–2013 and over (top) the other months.

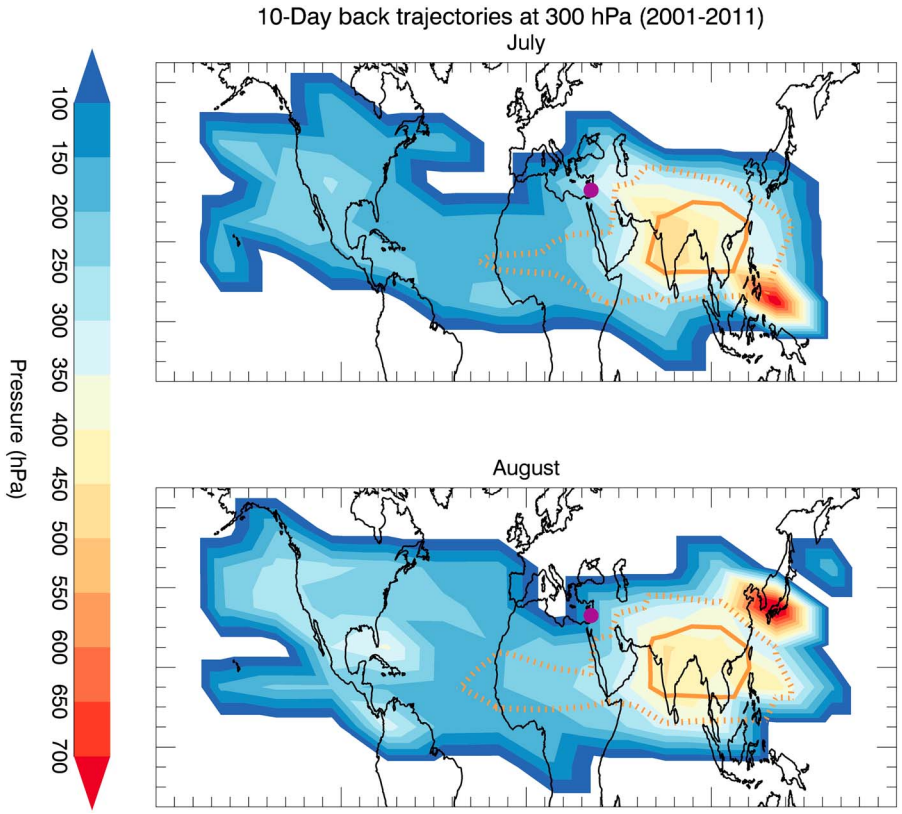

Figure 8. Pressure levels of air masses after 10 day back trajectories from the point located at 33°N, 35°E (purple filled circle) and 300 hPa in the eastern MB from the British Atmospheric Data Centre trajectory service (http://badc.Nerc.Ac.uk/community/trajectory/) in (top) July and in (bottom) August over the period of 2001–2011. The contour lines superimposed to the maps delimit the percentage of air masses reaching the eastern MB at 314 hPa after 10 days of transport: 55% (solid orange line) and 80% (dotted orange line).

(http://badc.nerc.ac.uk/community/trajectory/). The contour lines superimposed to the maps delimit the percentage of air masses reaching the eastern MB at 314 hPa after a transport of 10 days: 55% (solid orange line) and 80% (dotted orange line) of all trajectories (682 trajectories). Since 6 day back trajectories were sufficient to highlight the impact of the Indian subcontinent air masses on the MB [*Ricaud et al.*, 2014], we used 10 day back trajectories to detect the influence of planetary boundary layer sources.

The eastern MB air masses during summer come mostly from southeastern Asian and the Indian/Tibetan Plateau regions in July and August, as shown by the contour lines in Figure 8. However, air masses from the Indian subcontinent come from lower levels (500–550 hPa), whereas those from southeastern Asia come from upper levels (350–400 hPa). The so-called Asian monsoon anticyclone is actually an upper level divergence zone linked to the monsoon convective system and causes strong updrafts in the troposphere [*Randel and Park*, 2006]. Thus, air masses that have their origins in the Indian subcontinent are likely influenced by the boundary layer in the short term (less than 1 month) via the updrafts associated with the upper level divergence zone (referred to as monsoon anticyclone). Figure 9 represents the monthly averaged Asian N_2O emission fluxes used in LMDz-OR-INCA simulations superimposed with the contour lines in Figure 8. The peak of Asian N_2O emissions occurs in July, consistent with the peak of the east-west difference measured by GOSAT and calculated by LMDz-OR-INCA (Figure 6). There are two main regions of emissions: in northern India and in eastern China. The main emission region from eastern China is outside, while the northern Indian region is well inside the contour lines delimiting the main regions of origin of eastern MB air masses. This confirms the fact that upper tropospheric N_2O over the eastern MB in July and August comes mostly from Indian subcontinent N_2O emissions. This hypothesis is consistent with previous work on the Asian monsoon anticyclone composition in July and in August. First, *Vogel et al.* [2015] show that, in July 2012, the contribution of boundary layer sources to the Asian monsoon composition is between 35% and 55% and the

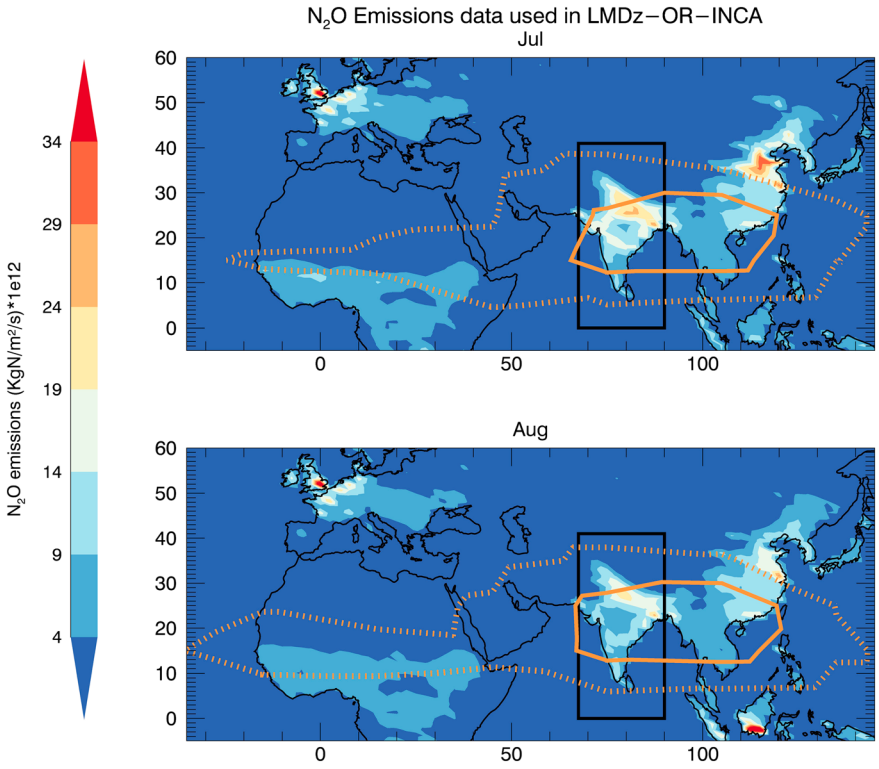

Figure 9. Monthly averaged Asian N_2O surface emission fluxes (kg m^{-2} s^{-1}) used in LMDz-OR-INCA simulations in (top) July and in (bottom) August. The black rectangle (0–41°N, 67.5–90°E) delimits the Indian subcontinent N_2O emission region. The contour lines (see Figure 8) delimit the percentage of air masses reaching the eastern MB at 314 hPa after 10 days of transport: 55% (solid orange line) and 80% (dotted orange line).

contributions of the Indian/Tibetan Plateau region and eastern China are 24% and 10%, respectively. Consequently, in July, the Indian/Tibetan Plateau and eastern China represent 43–68% and 18–28% of the contribution from all boundary layer sources to the Asian monsoon anticyclone, respectively. Second, *Bergman et al.* [2013] show that, in August 2011, the main contributions from the boundary layer sources to the Asian monsoon anticyclone composition are from India/Southeast Asia and the Tibetan Plateau regions (70–80%).

In summary, we showed the predominant contribution of the Indian subcontinent N_2O emissions on the composition of upper tropospheric N_2O over the eastern MB in July and in August. In the next section, we explain the biochemical processes involved in these N_2O emissions.

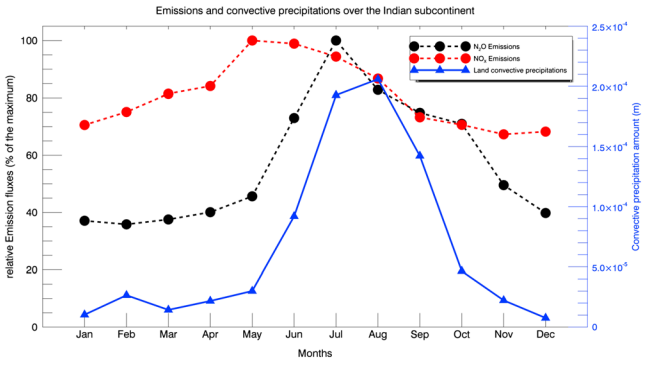

Figure 10. Seasonal variation of monthly averaged N_2O (black) and NO_x (red) relative to surface emission fluxes (emission fluxes divided by the maximum fluxes) used in LMDz-OR-INCA and the convective precipitation amount from the reanalysis ERA-Interim (blue) averaged over the Indian subcontinent (land pixels within the black box of Figure 9). The convective precipitation data are monthly averaged over the period of 2010–2013.

3.4. Emission Processes

The east-west difference of N_2O from GOSAT and LMDz-OR-INCA exhibits a maximum in summer peaking in July, namely, 1 month earlier than the occurrence of a CH_4 maximum analyzed by *Ricaud et al.* [2014]. This is due to environmental parameters such as soil moisture that influence N_2O emissions. Soil ability to emit N_2O can be characterized by analyzing the nitrification and the denitrification processes [*Qu et al.*, 2014]. Since intensified agriculture, characterized by high nitrogen fertilizer

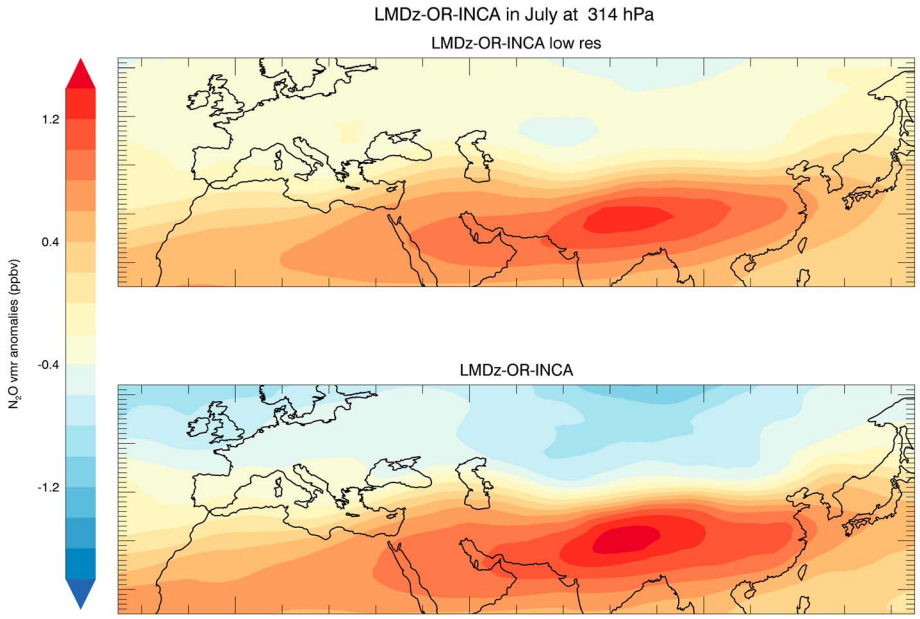

Figure 11. Monthly averaged N_2O volume mixing ratio anomaly (ppbv) from (top) LMDz-OR-INCA *low res* and (bottom) LMDz-OR-INCA at 314 hPa in July over the period of 2010–2013.

levels, are replacing traditional farming in many South Asian countries [*Rasul and Thapa*, 2003], the denitrification process is enhanced by the use of nitrogen fertilizers leading to an increase of N_2O emissions to the atmosphere [*Solomon et al.*, 2007]. N_2O emissions are positively correlated with soil moisture [*Raut et al.*, 2015], and the relative soil nitrogen emissions (NO, HONO, and N_2O) critically depend on the SWC [*Oswald et al.*, 2013] favoring NO and HONO when SWC ranges from 5 to 40% and favoring N_2O when SWC ranges from 40 to 70%. Thus, the South Asian region is a hot spot of N_2O emissions, especially during summertime when high precipitation events occur. Figure 10 shows the convective precipitation from the reanalysis ERA-Interim [*Dee et al.*, 2011] over the Indian subcontinent (land pixels within the black box in Figure 9) and the monthly averaged N_2O and nitrogen oxide (NO_x) emission fluxes used in LMDz-OR-INCA in this region. In addition to the rainfall information, the convective precipitation can be considered as a footprint of the presence and intensity of the updrafts associated with the Indian monsoon. The Indian subcontinent convective precipitation shows a maximum in July–August. The N_2O surface emissions over this region are highly correlated with precipitation with a maximum in summer and peaking in July. Actually, NO_x emissions peak in May–June, while N_2O emissions peak 1 month later in July (Figure 10). This time lag results from the processes occurring in the soil. Prior to the monsoon period, when SWC is low, a large amount of fertilizer is used in the Indian subcontinent and the surplus of nitrogen in soil mostly produces emissions of the nitrogen compounds NO and HONO. The emissions of NO are represented by NO_x emissions since NO is predominant in emissions of NO_x from soil [*Bertram et al.*, 2005]. During the Indian monsoon period, intense precipitation increases the soil humidity, and once the SWC reaches ~40% [*Oswald et al.*, 2013], N_2O becomes the dominant nitrogen compound emitted. Thus, if a peak in NO_x emissions is reached in June [*Ghude et al.*, 2010] through nitrification processes, it takes few days or weeks for the soil to have enough humidity over the entire Indian subcontinent and for microbial processes to get involved in the production and release of N_2O in the atmosphere through nitrification and denitrification processes [*Smith and Tiedje*, 1979]. This explains the July peak in N_2O emissions. Consequently, the measurements of N_2O in the upper troposphere over the eastern MB in summer (June-July-August, JJA) can be considered as a footprint of the N_2O emissions over the Asian and especially the Indian subcontinent regions. This is all the more interesting, as this region is difficult to observe from space in summer because of cloudy conditions associated with the monsoon system. It is valuable to examine another source of information to estimate the accumulation of N_2O in the Asian monsoon anticyclone and then to improve the estimation of N_2O emissions from agriculture over Asia.

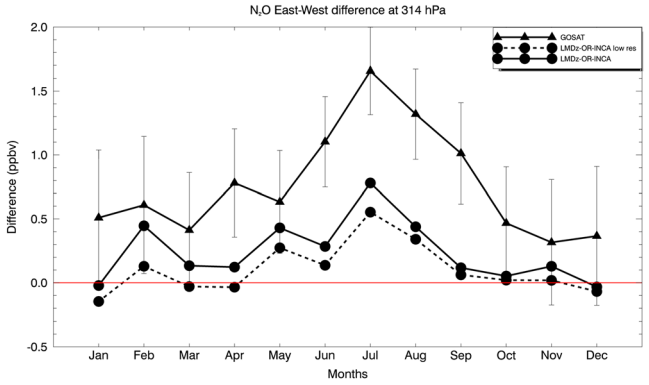

Figure 12. Seasonal variation of the east-west difference of N_2O (ppbv) measured by GOSAT/TANSO-FTS (solid line with triangles) and calculated by LMDz-OR-INCA (solid line with circles) and LMDz-OR-INCA *low res* (dashed line with circles) at 314 hPa over the period of 2010–2013. The error bars represent the error on the mean considering the total random errors of the retrieval and the number of monthly averaged values.

4. Discussion

Although measured and modeled east-west differences peak in July (Figure 6), the amplitude is twice as large in the GOSAT measurements than in the model outputs. To understand the possible reasons of these differences, we studied some parameters that impact the east-west difference in the model and in the GOSAT data sets.

In the model data, the east-west difference is affected by at least two factors: the emission sources, including the magnitude of emissions as well as the spatial distribution, and the horizontal resolution of the transport model.

To illustrate the impact of the horizontal resolution and the emission sources on the estimated east-west difference, we have compared the results from two different configurations of the model (LMDz-OR-INCA and LMDz-OR-INCA *low res*) as described in section 2.3. The global total emission rate in LMDz-OR-INCA is about 23% greater than in LMDz-OR-INCA *low res*. Over the Indian subcontinent (black box in Figure 9) in July, the emission rate in LMDz-OR-INCA is about 7% higher than in LMDz-OR-INCA *low res*. Figure 11 shows the northern hemisphere N_2O anomaly in July 2010–2013 at 314 hPa for LMDz-OR-INCA and LMDz-OR-INCA *low res*, and Figure 12 shows the east-west difference of GOSAT, LMDz-OR-INCA, and LMDz-OR-INCA *low res*. The N_2O vmr maxima and gradient in the Asian monsoon are more intense in LMDz-OR-INCA than in LMDz-OR-INCA *low res*. Consistently, the peak-to-peak amplitude of the east-west difference (Figure 12) is more intense in LMDz-OR-INCA (~0.8 ppbv) than in LMDz-OR-INCA *low res* (0.7 ppbv).

Since there is still a significant difference between the peak-to-peak amplitudes observed by GOSAT and calculated by LMDz-OR-INCA (1.8 ppbv and 1.5 ppbv, respectively), the N_2O emission fluxes could be larger over Asia than the fluxes fixed in the emission inventory used by LMDz-OR-INCA. The inaccurate understanding of some processes such as soil acidification involved in soil N_2O emission leads generally to an underestimation of the emission factor used to estimate soil emissions from agriculture [*Raut et al.*, 2015]. Consequently, this generates an underestimation of N_2O emission fluxes, which are linearly affected by the emission factors [*Dobbie et al.*, 1999]. There is also evidence of an underestimation of N_2O emissions at very high N-fertilizer application rates due to a nonlinear relationship between N-fertilizer and N_2O emissions [*Shcherbak et al.*, 2014].

In addition to the emission sources, the horizontal resolution of the model could likely play a role in the model east-west difference. *Bergman et al.* [2013] showed that the contribution of Indian boundary layer sources to the Asian monsoon anticyclone composition in August is less intense for a lower resolution of the dynamical model. This is due to the fact that the finer the horizontal resolution, the better the representation of mesoscale convection and therefore the more efficient the vertical transport processes to bring N_2O-enriched air masses into the upper troposphere. Moreover, the horizontal transport of air masses is also improved and better represented in the high-resolution model than in the coarser resolution model.

In the GOSAT data, the east-west difference is affected by the vertical sensitivity of the measurements. As we have already noted in section 2.2, applying GOSAT optimal estimation formalism (cf. equation (1)) to HIPPO measurements significantly reduces N_2O variability. Thus, to assess the impact of the vertical sensitivity of the measurements (represented by the averaging kernels in Figure 1) on the observed east-west difference, we applied the GOSAT averaging kernels to LMDz-OR-INCA outputs by using equation (1). The result in terms of east-west difference is shown in Figure 13. The smoothing of the model's vertical resolution by the application of GOSAT averaging kernels tends to reduce the variations in east-west difference. Although the difference still peaks in July, the peak-to-peak amplitude decreases from 0.8 to 0.4 ppbv. Actually, the east-west

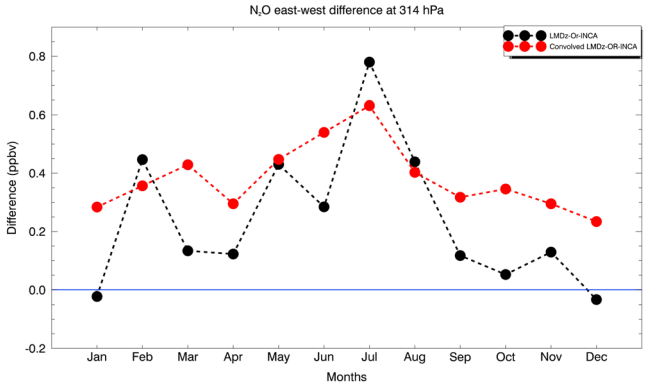

Figure 13. Seasonal variations of the east-west differences calculated by LMDz-OR-INCA (black) and LMDz-OR-INCA convolved by the GOSAT averaging kernels (red) monthly averaged over the period of 2010–2013.

differences are higher all year long in the convolved model than in the original, but the peak in July is less marked in the convolved model than in the original. These changes in the seasonal variability of the east-west difference can be understood when analyzing the broad width of the 314 hPa averaging kernel peak (Figure 1). The convolved LMDz-OR-INCA N_2O data at 314 hPa are also sensitive to higher and lower levels. Since the N_2O east-west difference variability is smaller in LMDz-OR-INCA at lower levels (e.g., a peak-to-peak amplitude of ~0.2 ppbv at 502 hPa, not shown) than in the upper troposphere, the impact of lower levels tends to decrease the variability of the east-west difference at 314 hPa. Moreover, because the western MB is located at higher latitudes than the eastern MB (see Figure 4), the convolved model at 200 hPa is influenced more by stratospheric N_2O in the western MB than in the eastern MB. Since N_2O vmr decreases with height in the stratosphere, the impact of the influence of stratospheric N_2O tends to increase the east-west difference at 314 hPa all year long. Similarly, we can consider that the amplitude of the east-west difference variations observed in GOSAT underestimates the real variations in amplitude and the positive east-west difference observed all year long is also likely due to the vertical sensitivity of the GOSAT measurements.

5. Conclusion

We used global-scale measurements of upper tropospheric N_2O from the GOSAT TANSO-FTS satellite instrument and outputs from the chemical transport model LMDz-OR-INCA to evaluate the impact of the Asian N_2O emissions on the N_2O distribution in the MB during summer. We assessed the quality of the GOSAT upper tropospheric N_2O retrievals by using the HIPPO airborne campaigns. This validation indicated an SD error of about 2.0 ppbv for a single pixel and a mean bias of about −1.3 ppbv (approximately −0.4%). Since we used monthly and regional means, this SD error is reduced to ~0.1 ppbv. The SD error deduced from the comparisons with HIPPO data is about 3 times less than the theoretical random errors used in this paper to analyze the significance of the seasonal variations.

The GOSAT and LMDz-OR-INCA monthly averaged upper tropospheric N_2O (2010–2013) over the MB have a significant seasonal cycle with a strong increase in summer. The eastern MB is highly enriched in N_2O producing a peak in July in the east-west difference of N_2O over the MB as calculated by the model and as observed by GOSAT. This is due to the impact of air masses originated from Asia and transported over the eastern MB through the Asian monsoon anticyclone. Back trajectory calculations also showed that the main sources of eastern MB upper tropospheric N_2O in summer come from the Indian subcontinent region where high emissions occur during the monsoon period. These high N_2O emissions are due to the high precipitation associated with the monsoon and combined with heavy use of fertilizers, since N_2O emissions occur under conditions of high SWC.

Since the summertime maximum over the eastern MB is linked to the maximum of N_2O surface emissions over Asia and mainly the Indian subcontinent, the eastern MB can therefore be used as a footprint of summertime N_2O emissions over this region. However, the east-west difference peak in July is almost twice as large in GOSAT (~1.4 ppbv) than in LMDz-OR-INCA (~0.8 ppbv). This is likely due to an underestimation of the N_2O Indian subcontinent emission sources and a relatively coarse horizontal resolution in the model that affects the efficiency of the vertical transport within the Asian monsoon Anticyclone. In addition, the application of the averaging kernels from GOSAT to the model tends to reduce the east-west N_2O difference variations likely due to the low vertical sensitivity of the satellite measurements (represented by the averaging kernel).

One major outcome of this study is that the use of current GOSAT N_2O measurements over the MB can help to improve the estimation of N_2O emissions over Asia and especially the Indian subcontinent in a top-down emission estimation strategy. Moreover, tropospheric N_2O satellite measurements are made difficult in summer over Asia due to cloudy conditions associated with the monsoon period. In such case, upper tropospheric N_2O measurements over the MB could be the best alternative to estimate the N_2O accumulation in the Asian summer monsoon anticyclone and then to assess the surface emissions that caused this accumulation.

Acknowledgments
We would like to thank the following institutes and programs for funding our study: Centre National de la Recherche Scientifique-Institut National des Sciences de l'Univers (CNRS-INSU), Centre National des Etudes Spatiales (CNES), Agence de l'Environnement et de la Maîtrise de l'Energie (ADEME) through the program the Mediterranean Integrated Studies at Regional And Local Scales (MISTRALS), Chemistry-Aerosol Mediterranean Experiment (ChArMEx), Météo-France, and Airbus Defense and Space for funding Y. Kangah's PhD thesis and the Greenhouse gases Observing SATelite (GOSAT) Research Announcement (RA) Initiative. The GOSAT N_2O data can be obtained by contacting Naoko Saitoh via e-mail at nsaitoh@faculty.chiba-u.jp. The chemical model INCA can be downloaded from http://forge.ipsl.jussieu.fr/inca, and the LMDz-OR-INCA N_2O data used in this paper can be obtained by contacting Didier Hauglustaine via e-mail at didier.hauglustaine@lsce.ipsl.fr. We finally would like to thank the three anonymous reviewers for their fruitful comments.

References

Bergman, J. W., F. Fierli, E. J. Jensen, S. Honomichl, and L. L. Pan (2013), Boundary layer sources for the Asian anticyclone: Regional contributions to a vertical conduit, *J. Geophys. Res. Atmos.*, *118*, 2560–2575, doi:10.1002/jgrd.50142.

Bertram, T. H., A. Heckel, A. Richter, J. P. Burrows, and R. C. Cohen (2005), Satellite measurements of daily variations in soil NO_x emissions, *Geophys. Res. Lett.*, *32*, L24812, doi:10.1029/2005GL024640.

Bouwman, A., and J. Taylor (1996), Testing high-resolution nitrous oxide emission estimates against observations using an atmospheric transport model, *Global Biogeochem. Cycles*, *10*(2), 307–318, doi:10.1029/96GB00191.

Butterbach-Bahl, K., and M. Dannenmann (2011), Denitrification and associated soil N_2O emissions due to agricultural activities in a changing climate, *Curr. Opin. Environ. Sustainability*, *3*(5), 389–395, doi:10.1016/j.cosust.2011.08.004.

Butterbach-Bahl, K., E. M. Baggs, M. Dannenmann, R. Kiese, and S. Zechmeister-Boltenstern (2013), Nitrous oxide emissions from soils: How well do we understand the processes and their controls?, *Philos. Trans. R. Soc. London, Ser. B*, *368*(1621), 20,130,122, doi:10.1098/rstb.2013.0122.

Ciais, P., et al. (2014), Carbon and other biogeochemical cycles, in *In Climate Change 2013: The Physical Science Basis. Contribution of Working Group I to the Fifth Assessment Report of the Intergovernmental Panel on Climate Change*, pp. 465–570, Cambridge Univ. Press, Cambridge, U. K.

Claeyman, M., et al. (2011), A geostationary thermal infrared sensor to monitor the lowermost troposphere: O_3 and co retrieval studies, *Atmos. Meas. Tech.*, *4*(2), 297–317, doi:10.5194/amt-4-297-2011.

Dayan, U. (1986), Climatology of back trajectories from Israel based on synoptic analysis, *J. Clim. Appl. Meteorol.*, *25*(5), 591–595, doi:10.1175/1520-0450(1986)025.

Dee, D., et al. (2011), The ERA-Interim reanalysis: Configuration and performance of the data assimilation system, *Q. J. R. Meteorol. Soc.*, *137*(656), 553–597, doi:10.1002/qj.828.

Dobbie, K., I. McTaggart, and K. Smith (1999), Nitrous oxide emissions from intensive agricultural systems: Variations between crops and seasons, key driving variables, and mean emission factors, *J. Geophys. Res.*, *104*(D21), 26,891–26,899, doi:10.1029/1999JD900378.

Eguchi, N., and T. Yokota (2008), Investigation of clearsky occurrence rate estimated from CALIOP and MODIS observations, *Geophys. Res. Lett.*, *35*, L23816, doi:10.1029/2008GL035897.

Ghude, S. D., D. Lal, G. Beig, R. van der A, and D. Sable (2010), Rain-induced soil NO_x emission from India during the onset of the summer monsoon: A satellite perspective, *J. Geophys. Res.*, *115*, D16304, doi:10.1029/2009JD013367.

Giglio, L., J. T. Randerson, and G. R. Werf (2013), Analysis of daily, monthly, and annual burned area using the fourth-generation global fire emissions database (GFED4), *J. Geophys. Res. Biogeosci.*, *118*, 317–328, doi:10.1002/jgrg.20042.

Hamazaki, T., Y. Kaneko, A. Kuze, and K. Kondo (2005), Fourier transform spectrometer for Greenhouse gases Observing SATellite (GOSAT), in Fourth International Asia-Pacific Environmental Remote Sensing Symposium 2004: Remote Sensing of the Atmosphere, Ocean, Environment, and Space, pp. 73–80, International Society for Optics and Photonics, doi:10.1117/12.581198.

Hauglustaine, D., F. Hourdin, L. Jourdain, M.-A. Filiberti, S. Walters, J.-F. Lamarque, and E. Holland (2004), Interactive chemistry in the laboratoire de météorologie dynamique general circulation model: Description and background tropospheric chemistry evaluation, *J. Geophys. Res.*, 109, D04314, doi:10.1029/2003JD003957.

Hauglustaine, D., Y. Balkanski, and M. Schulz (2014), A global model simulation of present and future nitrate aerosols and their direct radiative forcing of climate, *Atmos. Chem. Phys.*, *14*(5), 11,031–11,063, doi:10.5194/acp-14-11031-2014.

Ishida, H., and T. Y. Nakajima (2009), Development of an unbiased cloud detection algorithm for a spaceborne multispectral imager, *J. Geophys. Res.*, *114*, D07206, doi:10.1029/2008JD010710.

Ishida, H., T. Y. Nakjima, T. Yokota, N. Kikuchi, and H. Watanabe (2011), Investigation of GOSAT TANSO-CAI cloud screening ability through an intersatellite comparison, *J. Appl. Meteorol. Climatol.*, *50*(7), 1571–1586, doi:10.1175/2011JAMC2672.1.

Kort, E., et al. (2011), Tropospheric distribution and variability of N_2O: Evidence for strong tropical emissions, *Geophys. Res. Lett.*, *38*, L15806, doi:10.1029/2011GL047612.

Krinner, G., N. Viovy, N. de Noblet-Ducoudre, J. Ogee, J. Polcher, P. Friedlingstein, P. Ciais, S. Sitch, and I. C. Prentice (2005), A dynamic global vegetation model for studies of the coupled atmosphere-biosphere system, *Global Biogeochem. Cycles*, *19*, GB1015, doi:10.1029/2003GB002199.

Kuze, A., H. Suto, M. Nakajima, and T. Hamazaki (2009), Thermal and near infrared sensor for carbon observation Fourier-transform spectrometer on the Greenhouse gases Observing SATellite for greenhouse gases monitoring, *Appl. Opt.*, *48*(35), 6716–6733, doi:10.1364/AO.48.006716.

Minschwaner, K., R. Salawitch, and M. McELroy (1993), Absorption of solar radiation by O_2: Implications for O_3 and lifetimes of N_2O, $CFCL_3$ and CF_2CL_2, *J. Geophys. Res.*, *98*(D6), 10,543–10,561, doi:10.1029/93JD00223.

Oswald, R., et al. (2013), HONO emissions from soil bacteria as a major source of atmospheric reactive nitrogen, *Science*, *341*(6151), 1233–1235, doi:10.1126/science.1242266.

Qu, Z., J. Wang, T. Almøy, and L. R. Bakken (2014), Excessive use of nitrogen in Chinese agriculture results in high $N_2O/(N_2O + N_2)$ product ratio of denitrification, primarily due to acidification of the soils, *Global Change Biol.*, *20*(5), 1685–1698, doi:10.1111/gcb.12461.

Randel, W. J., and M. Park (2006), Deep convective influence on the Asian summer monsoon anticyclone and associated tracer variability observed with Atmospheric Infrared Sounder (AIRS), *J. Geophys. Res.*, *111*, D12314, doi:10.1029/2005JD006490.

Rasul, G., and G. Thapa (2003), Shifting cultivation in the mountains of South and Southeast Asia: Regional patterns and factors influencing the change, *Land Degrad. Dev.*, *14*(5), 495–508, doi:10.1002/ldr.570.

Raut, N., B. K. Sitaula, L. R. Bakken, R. M. Bajracharya, and P. Dörsh (2015), Higher N_2O emission by intensified crop production in South Asia, *Global Ecol. Conserv.*, *4*, 176–184, doi:10.1016/j.gecco.2015.06.004.

Ravishankara, A., J. S. Daniel, and R. W. Portmann (2009), Nitrous oxide (N_2O): The dominant ozone-depleting substance emitted in the 21st century, *Science*, *326*(5949), 123–125, doi:10.1126/science.1176985.

Ricaud, P., J.-L. Attié, H. Teyssedre, L. E. Amraoui, V.-H. Peuch, M. Matricardi, and P. Schluessel (2009), Equatorial total column of nitrous oxide as measured by IASI on METOP-A: Implications for transport processes, *Atmos. Chem. Phys.*, *9*(12), 3947–3956, doi:10.5194/acp-9-3947-2009.

Ricaud, P., et al. (2014), Impact of the Asian monsoon anticyclone on the variability of mid-to-upper tropospheric methane above the Mediterranean Basin, *Atmos. Chem. Phys.*, *14*(20), 11,427–11,446, doi:10.5194/acp-14-11427-2014.

Rodgers, C. D. (2000), *Inverse Methods for Atmospheric Sounding: Theory and Practice*, vol. 2, pp. 43–63, World scientific, Singapore.

Rodwell, M. J., and B. J. Hoskins (1996), Monsoons and the dynamics of deserts, *Q. J. R. Meteorol. Soc.*, *122*(534), 1385–1404, doi:10.1002/qj.49712253408.

Saitoh, N., R. Imasu, Y. Ota, and Y. Niwa (2009), CO_2 retrieval algorithm for the thermal infrared spectra of the Greenhouse gases Observing SATellite: Potential of retrieving CO_2 vertical profile from high-resolution FTS sensor, *J. Geophys. Res.*, 114, D17305, doi:10.1029/2008JD011500.

Saitoh, N., et al. (2016), Algorithm update of the GOSAT/TANSOFTS thermal infrared CO_2 product (version 1) and validation of the UTLS CO_2 data using contrail measurements, *Atmos. Meas. Tech.*, *9*(5), 2119–2134, doi:10.5194/amt-9-2119-2016.

Scheeren, H., et al. (2003), The impact of monsoon outflow from India and Southeast Asia in the upper troposphere over the eastern Mediterranean, *Atmos. Chem. Phys.*, *3*(5), 1589–1608, doi:10.5194/acp-3-1589-2003.

Shcherbak, I., N. Millar, and G. P. Robertson (2014), Global metaanalysis of the nonlinear response of soil nitrous oxide (N_2O) emissions to fertilizer nitrogen, *Proc. Natl. Acad. Sci. U.S.A.*, *111*(25), 9199–9204, doi:10.1073/pnas.1322434111.

Smith, M. S., and J. M. Tiedje (1979), Phases of denitrification following oxygen depletion in soil, *Soil Biol. Biochem.*, *11*(3), 261–267, doi:10.1016/0038-0717(79)90071-3.

Solomon, S., D. Qin, M. Manning, Z. Chen, M. Marquis, K. Averyt, M. Tignor, and H. Miller (2007), Contribution of working group I to the fourth assessment report of the Intergovernmental Panel on Climate Change, 2007.

Syakila, A., and C. Kroeze (2011), The global nitrous oxide budget revisited, *GHG Meas. Manage.*, *1*(1), 17–26, doi:10.3763/ghgmm.2010.0007.

Thompson, R. L., et al. (2014), Transcom N_2O model inter-comparison—Part 1: Assessing the influence of transport and surface fluxes on tropospheric N_2O variability, *Atmos. Chem. Phys.*, *14*(8), 4349–4368, doi:10.5194/acp-14-4349-2014.

Tsutsumi, Y., K. Mori, T. Hirahara, M. Ikegami, and T. J. Conway (2009), Technical report of global analysis method for major greenhouse gases by the World Data Center for Greenhouse Gases, WMO/TD, (1473).

Tyrlis, E., J. Lelieveld, and B. Steil (2013), The summer circulation over the eastern Mediterranean and the Middle East: Influence of the South Asian monsoon, *Clim. Dyn.*, *40*(5–6), 1103–1123, doi:10.1007/s00382-012-1528-4.

van der Werf, G. R., et al. (2010), Global fire emissions and the contribution of deforestation, savanna, forest, agricultural, and peat fires (1997–2009), *Atmos. Chem. Phys.*, *10*(23), 11,707–11,735, doi:10.5194/acp-10-11707-2010.

Vogel, B., G. Gunther, R. Muller, J.-U. Grooß, and M. Riese (2015), Impact of different Asian source regions on the composition of the Asian monsoon anticyclone and of the extratropical lowermost stratosphere, *Atmos. Chem. Phys.*, *15*(23), 13,699–13,716, doi:10.5194/acp-15-13699-2015.

Wofsy, S. C. (2011), HIAPER Pole-to-Pole Observations (HIPPO): Fine-grained, global-scale measurements of climatically important atmospheric gases and aerosols, *Philos. Trans. R. Soc. London A*, *369*(1943), 2073–2086, doi:10.1098/rsta.2010.0313.

Wofsy, S. C., et al. (2012), HIPPO merged 10-second meteorology, atmospheric chemistry, Aerosol data (R_20121129), Carbon Dioxide Inf. Anal. Cent., Oak Ridge Natl. Lab., Oak Ridge, Tenn., doi:10.3334/CDIAC/hippo_010.

Xiong, X., E. S. Maddy, C. Barnet, A. Gambacorta, P. K. Patra, F. Sun, and M. Goldberg (2014), Retrieval of nitrous oxide from Atmospheric Infrared Sounder: Characterization and validation, *J. Geophys. Res. Atmos.*, *119*, 9107–9122, doi:10.1002/2013JD021406.

Yokota, T., Y. Yoshida, N. Eguchi, Y. Ota, T. Tanaka, H. Watanabe, and S. Maksyutov (2009), Global concentrations of CO_2 and CH_4 retrieved from GOSAT: First preliminary results, *Sola*, *5*, 160–163, doi:10.2151/sola.2009-041.

Zander, R., E. Mahieu, P. Demoulin, P. Duchatelet, et al. (2005), Evolution of a dozen non-CO_2 greenhouse gases above central Europe since mid-1980s, *Environ. Sci.*, *2*(2–3), 295–303.